Journal of Atmospheric and Solar-Terrestrial Physics 146 (2016) 171–185

Contents lists available at ScienceDirect

Journal of Atmospheric and Solar-Terrestrial Physics

journal homepage: www.elsevier.com/locate/jastp

A small mission concept to the Sun–Earth Lagrangian L5 point for innovative solar, heliospheric and space weather science

B. Lavraud [a,b,*], Y. Liu [c], K. Segura [a,b], J. He [d], G. Qin [c], M. Temmer [e], J.-C. Vial [f], M. Xiong [c], J.A. Davies [g], A.P. Rouillard [a,b], R. Pinto [a,b], F. Auchère [f], R.A. Harrison [g], C. Eyles [g], W. Gan [h], P. Lamy [i], L. Xia [j], J.P. Eastwood [k], L. Kong [c], J. Wang [c], R.F. Wimmer-Schweingruber [l], S. Zhang [c], Q. Zong [d], J. Soucek [m], J. An [c], L. Prech [n], A. Zhang [c], P. Rochus [o], V. Bothmer [p], M. Janvier [f,q], M. Maksimovic [r], C.P. Escoubet [s], E.K.J. Kilpua [t], J. Tappin [g], R. Vainio [u], S. Poedts [v], M.W. Dunlop [g,w], N. Savani [x,y], N. Gopalswamy [y], S.D. Bale [z], G. Li [aa], T. Howard [ab], C. DeForest [ab], D. Webb [ac], N. Lugaz [ad], S.A. Fuselier [ae], K. Dalmasse [af], J. Tallineau [ag], D. Vranken [ag], J.G. Fernández [ah]

[a] Institut de Recherche en Astrophysique et Planétologie, Université de Toulouse (UPS), France
[b] Centre National de la Recherche Scientifique, UMR 5277, Toulouse, France
[c] National Space Science Center, Chinese Academy of Sciences, Beijing, China
[d] Peking University, Beijing, China
[e] Institute of Physics, University of Graz, Austria
[f] Institut d'Astrophysique Spatiale, Orsay, France
[g] RAL Space, Didcot, UK
[h] Purple Mountain Observatory, Nanjing, China
[i] Laboratoire d'Astrophysique de Marseille, CNRS & Aix-Marseille Université, France
[j] Shandong University, Weihai, China
[k] Imperial College, London, UK
[l] Christian Albrechts University, Kiel, Germany
[m] Institute of Atmos. Phys., Prague, Czech Republic
[n] Charles University, Prague, Czech Republic
[o] Centre Spatial de Liège, Belgium
[p] University of Gottingen, Germany
[q] Institut d'Astrophysique Spatiale, CNRS, Univ. Paris-Sud, Université Paris-Saclay, France
[r] Observatoire de Paris, Meudon, France
[s] European Space Agency, The Netherlands
[t] University of Helsinki, Finland
[u] University of Turku, Finland
[v] Katholieke Universiteit Leuven, Belgium
[w] Beihang University, Beijing, China
[x] UMBC, Goddard Planetary Heliophysics Institute (GPHI), University of Maryland, Baltimore, USA
[y] NASA Goddard Space Flight Center, USA
[z] University of California, Berkeley, USA
[aa] University of Alabama, Huntsville, USA
[ab] Southwest Research Institute, Boulder, USA
[ac] ISR, Boston College, Chestnut Hill, MA, USA
[ad] University of New Hampshire, USA
[ae] Southwest Research Institute, San Antonio, USA
[af] National Center for Atmospheric Research, Boulder, USA
[ag] Qinetiq Space, Kruibeke, Belgium
[ah] GMV, Tres Cantos, Spain

ARTICLE INFO

Article history:
Received 19 October 2015
Received in revised form
6 June 2016
Accepted 7 June 2016
Available online 8 June 2016

ABSTRACT

We present a concept for a small mission to the Sun–Earth Lagrangian L5 point for innovative solar, heliospheric and space weather science. The proposed INvestigation of Solar-Terrestrial Activity aNd Transients (INSTANT) mission is designed to identify how solar coronal magnetic fields drive eruptions, mass transport and particle acceleration that impact the Earth and the heliosphere. INSTANT is the first mission designed to (1) obtain measurements of coronal magnetic fields from space and (2) determine coronal mass ejection (CME) kinematics with unparalleled accuracy. Thanks to innovative instrumentation at a

* Corresponding author at: Institut de Recherche en Astrophysique et Planétologie, Université de Toulouse (UPS), France.

http://dx.doi.org/10.1016/j.jastp.2016.06.004

Keywords:
Space mission
Coronal mass ejections
Instrumentation
Space weather

vantage point that provides the most suitable perspective view of the Sun–Earth system, INSTANT would uniquely track the whole chain of fundamental processes driving space weather at Earth. We present the science requirements, payload and mission profile that fulfill ambitious science objectives within small mission programmatic boundary conditions.

1. Introduction

Coronal mass ejections (CMEs) are massive expulsions of plasma and magnetic flux from the solar corona into interplanetary space with speeds ranging from 200 to 3000 km/s. The occurrence rate of CMEs varies with the solar cycle, from 1 per day at solar minimum to 5 per day on average during solar maximum (e.g., Webb and Howard, 2012; and references therein). CMEs are recognized as the main drivers of detrimental space weather effects at Earth and in the heliosphere. They are the main cause of major geomagnetic storms resulting in large ionospheric and ground-induced currents which can disrupt satellite operations, navigation systems, radio communications and ground power grids (e.g., Schrijver et al., 2015). Moreover, together with large flares, they are responsible for the most intense solar energetic particle events, which can endanger life and disrupt technology on the Earth and in space (e.g., Reid, 1986). The motivation of the INSTANT mission concept arises from a basic fact: our current inability to understand how and when a CME will erupt, whether or not a CME has any chance of impacting the Earth, and to what degree it can disturb the near-Earth space environment. The INSTANT design is based on the realization that some of these open questions can be resolved within a small mission programmatic constraint, with innovative observations from a vantage point that provides a comprehensive view of (1) the processes at the Sun known to drive severe space weather at Earth and (2) the region of space between the Sun and the Earth (cf. Fig. 1).

Interest in observing solar-terrestrial phenomena from the Lagrangian L4 and L5 points comes from the suitability of these locations for tracking disturbances that propagate towards the Earth. The only mission that has actually performed measurements from these locations was NASA's STEREO mission (Kaiser et al., 2008), comprising two identical spacecraft drifting ahead of and behind the Earth on similar orbits around the Sun. These spacecraft only drifted through the L4 and L5 points, and did not station-keep there for continuous observations of Earth-impacting transients.

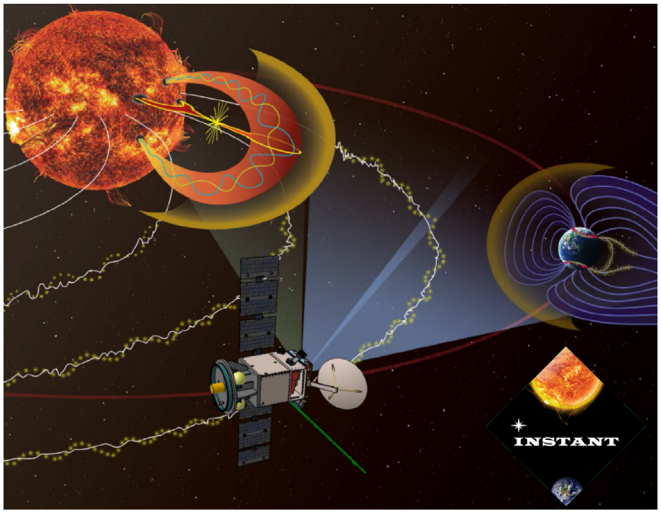

Fig. 1. Artistic view of the INSTANT mission concept.

Despite this, the STEREO mission paved the way for future L5/L4 dedicated missions. It demonstrated the capability of wide-angle, white-light imaging (Heliospheric Imagers; HI; Eyles et al., 2009) to track density disturbances from Thomson scattering off heliospheric electrons all the way from the Sun to the Earth, as well as other space weather capabilities (e.g., Simunac et al., 2009; Webb et al., 2010). Both L4 and L5 are good locations for tracking Earth-bound CMEs. However, as further detailed throughout the paper, for a single spacecraft mission the L5 location is more appropriate as it provides early observation of active regions, coronal holes and corotating interaction regions owing to solar rotation.

Other L5 mission concepts have been suggested and proposed in the recent past, but with different focus owing to different instrumentation and programmatic constraints. We note in particular the early concept summarized in Schmidt and Bothmer (1996), and which was submitted to the ESA medium class mission call in 1993. The concept resembled INSTANT in that it had a limited payload budget, albeit with different instrumentation, science goals and mission profile. A small mission concept was also presented in Akioka et al. (2005), focusing primarily on ways to achieve wide-angle interplanetary imaging and efficient on-board data processing (given the limited telemetry available from L5).

Larger L5 mission concepts have been proposed more recently, with in particular the Earth-Affecting Solar Causes Observatory (EASCO; Gopalswamy et al., 2011a, 2011b). This mission concept proposes to fill the gaps in observational capabilities of past missions (e.g., SOHO and STEREO), with key additional measurements such as radio, magnetograph and X-ray imaging. EASCO was studied in detail by NASA, including the full mission profile that differs greatly from that of INSTANT owing to EASCO's much broader payload. Strugarek et al. (2015) also recently proposed a large mission concept for both space weather science and operational purposes, with two spacecraft separated by 34° east and west from the Earth on its orbit for stereoscopic imaging of Earth-bound disturbances. The importance of an L5 mission for space weather purposes was recently presented by Vourlidas (2015), as well as in the COSPAR and ILWS roadmap (Schrijver et al., 2015).

With INSTANT, we propose a specific L5 mission concept focused primarily on science, with innovative instrumentation on board a small platform, and with an efficient mission profile to comply with a small mission opportunity. The baseline payload consists of 5 complementary instruments. The MAGIC (MAGnetic Imager of the Corona) coronagraph would for the first time provide measurements from space of the coronal magnetic field from 1.15 to 3 solar radii (R_S), using polarization measurements in the Lyman-α line (through the Hanle effect). It also would obtain white-light imaging. The Polarizing HELiospheric Imager eXplorer (PHELIX) performs wide-angle (out to 70° elongation from Sun center) imaging in the white-light domain with unprecedented polarization capabilities. The baseline payload also comprises a set of three complementary in-situ instruments, with an associated In-situ Data Processing Unit (IDPU): MAG (MAGnetometer), PAS (Proton and Alpha Sensor) and HEPS (High Energy Particle Sensor).

2. Science objectives

The science objectives of the INSTANT mission concept are summarized in Table 1, and detailed science argumentation for

such a design is provided in the following sections.

These science questions follow from the overall mission objective of improving our understanding of the processes at the Sun pertinent to space weather at Earth, and are themselves topical scientific questions. It can be noted that the proposed concept and instrumentation directly satisfy the need for "3D mapping of solar field involved in eruptions", "Mapping the global solar field", "Determination of the foundation of the heliospheric field", and "Solar energetic particles in the inner heliosphere" expressed by the COSPAR/ILWS Roadmap (cf. Appendix F.2, F.5, F.6 and F.9 of Schrijver et al. (2015)).

2.1. What is the coronal magnetic field configuration before and during CME eruptions?

Because coronal dynamics is dominated by its magnetic field, knowledge of its structure is critical to better constrain solar and heliospheric physics (e.g., Gary, 2001; Aschwanden, 2004; Mackay and Yeates, 2012). However, until now there have been no direct measurements of coronal magnetic fields, apart from a few ground-based efforts with significant limitations. Ground-based measurements of low-lying active regions have used the Hanle effect in infrared lines with a coarse resolution and over a limited field-of-view (FOV), typically only up to $1.5R_S$ at most (Tomczyk et al., 2008). Some isolated attempts to use the Zeeman effect have also been made (Lin et al., 2004). Another method based on shock standoff-distance has shown promise (Gopalswamy and Yashiro, 2011), but can be used only in the vicinity of CME-driven shocks and is strongly affected by projection effects. INSTANT provides a means by which to obtain coronal magnetic fields out to large distances, with capabilities well beyond current ground-based observations.

CME studies have led to more than a dozen theoretical models, which provide specific scenarios of the situation before, during and after the eruption of the CME (see reviews by Fan (2015) and Gibson (2015)). The ongoing debate stems from the lack of observational constraints of the dominant coronal magnetic fields before and during the CME eruptions that control CME formation and early dynamics. Most coronal and CME magnetic field models rely upon the extrapolation of photospheric magnetic measurements to infer the coronal magnetic field. However, the photosphere only constitutes the solar surface where coronal field lines are rooted (cf. Fig. 2; e.g., Amari et al., 2014). Moreover, the plasma regime is different in these two regions: the photosphere is plasma dominated (plasma $\beta \gg 1$), whereas the corona is magnetically dominated ($\beta \ll 1$; β is the ratio of the plasma to magnetic pressures). The situation is further complicated by the presence of the chromosphere and transition region between the photosphere and corona. Extrapolations based solely on photospheric observations thus result in large uncertainties in the modeled coronal magnetic field. A key structure involved in all CME models, and confirmed by in-situ observations, is a flux rope with possible current sheets and magnetic null points (see Fig. 2). It is still under debate whether this flux rope exists before the eruption or is formed during the eruption (Forbes et al., 2006).

2.1.1. Determining the magnetic field configuration of the corona

Light resulting from photons scattering off coronal ions is polarized because of the anisotropic incident radiation. The magnetic field has a depolarizing effect on the scattered light and this depolarization is measureable. It has been shown in particular that the polarization/depolarization of ultraviolet (UV) radiation by the magnetic field through the Hanle effect (Trujillo Bueno et al., 2005; Lopez-Ariste, 2015) provides an efficient tool for measuring the magnitude and orientation of the horizontal component of the coronal magnetic field. This technique appears to be applied best to measurements of the Lyman-α line, the brightest in the (far) UV domain, as shown by Bommier and Sahal-Bréchot (1982) and more recently by Trujillo Bueno et al. (2005). According to these studies, the polarization factor may be up to 25% at about one solar radius above the limb where the depolarization due to the magnetic field is easily detectable. The technique relies upon measurements of the linear polarization of the (line-of-sight-integrated) Lyman-α line, which is described by Derouich et al. (2010). The derivation of the coronal magnetic field requires a non-trivial procedure (forward modeling), although Derouich et al. (2010) have shown that the polarization signal is not lost through integration along the line of sight.

A major strength of such remote-sensing measurements is that they are performed over an extended field-of-view (FOV). This permits the building of maps of the coronal horizontal magnetic field properties to constrain the magnetic structure in the corona itself (i.e., in addition to photospheric magnetic field maps). Another strength is that relatively small magnetic fields (between 10 G and a few 100 G) are measureable; such values are typical of active regions extending to high altitudes (Dere, 1996; Mandrini et al., 2000). However, such solar observations may only be performed from space since the Lyman-α line is absorbed in the Earth's atmosphere. Observations from space can also be coupled with other polarization and coronal magnetic field measurements from the ground, e.g., Coronal Multi-channel Polarimeter (CoMP; Tomczyk et al., 2008) and Pic-du-Midi observations (e.g., Arnaud et al., 2006), with cross-calibration and benchmarking advantages.

Knowledge of the coronal magnetic field is most critical within the corona up to distances where it becomes essentially radial. Measurements of the magnetic field up to 2–3 solar radii combined with photospheric magnetic field maps as inputs to modeling and extrapolations would lead to a giant leap forward in our understanding of the coronal magnetic structure. A first measurement requirement (MR) (cf. summary in Tables 2 and 3) is thus to measure the coronal magnetic field, at least its horizontal component in the plane of the sky, with a sufficient spatial resolution and FOV (MR1) for such modeling purposes. Reconstructions from magnetograms made from Earth cannot be

Table 1
Summary of the INSTANT science questions, their subtopics and related sections.

Science question	Subtopics	Section
1. What is the coronal magnetic field configuration before and during CME eruptions?	Determining the magnetic field configuration of the corona	2.1.1
	Characterizing the coronal structure associated with CME initiation processes	2.1.2
2. What controls CME acceleration and subsequent propagation in the inner heliosphere?	Connecting coronal magnetic field restructuring with early CME dynamics	2.2.1
	Disentangling CME Sun-to-Earth kinematics from projection and geometric effects	2.2.2
	Comparing CME remote-sensing characteristics with in-situ measurements	2.2.3
3. Where do CME-driven shocks form and how do their properties affect particle acceleration?	Determining shock formation and properties	2.3.1
	Measuring energetic particle spectra in relation to shock properties	2.3.2
4. How do observations at L5 increase our space weather prediction capabilities?	Advance determination of CME arrival, geo-effective Bz, co-rotating interaction regions (CIRs) and solar energetic particles (SEPs)	2.4

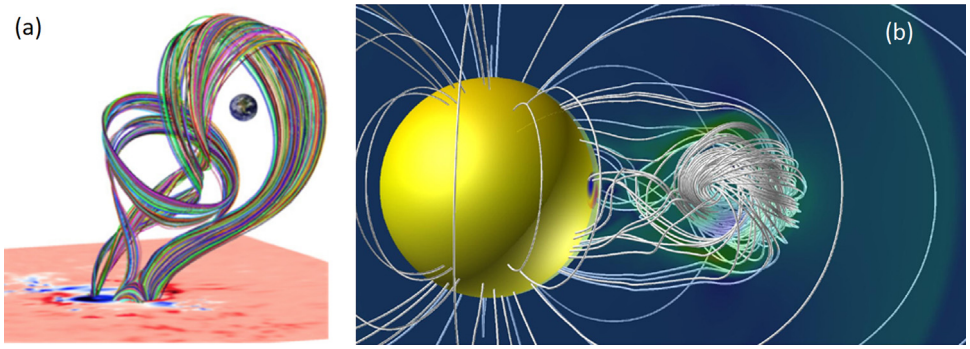

Fig. 2. (a) A model of an expanding flux rope leading to a CME, based on photospheric measurements (Amari et al., 2014). The Earth is illustrated at its true scale. (b) 3D MHD modeling of a CME eruption in the corona (credit: joint project for space weather modeling). Such modeling efforts are not constrained by current coronal magnetic field measurements.

Table 2
INSTANT science traceability matrix.

Science question	Subtopic	Measurement Requirements											
		MR 1	MR 2	MR 3	MR 4	MR 5	MR 6	MR 7	MR 8	MR 9	MR 10	MR 11	MR 12
1. What is the coronal magnetic field configuration before and during CME eruptions?	1.1 Coronal magnetic structure	✓											
	1.2 CME initiation	✓	✓	✓	✓	✓							
2. What controls CME acceleration and subsequent propagation in the inner heliosphere?	2.1 Early CME dynamics	✓	✓	✓									
	2.2 Heliospheric CME kinematics						✓	✓	✓	✓			
	2.3 Comparison with in-situ data				✓		✓	✓	✓	✓	✓	✓	
3. Where do CME-driven shocks form and how do their properties affect particle acceleration?	3.1 Shock formation and properties	✓	✓	✓			✓	✓	✓	✓			
	3.2 Particle acceleration at shocks	✓	✓	✓	✓		✓	✓	✓	✓	✓	✓	✓
4. INSTANT space weather capability	4.1 – 4.4	✓	✓	✓	✓	✓	✓	✓	✓	✓	✓	✓	✓

Table 3
INSTANT traceability matrix showing how the science measurement requirements translate into the instrument performance requirements.

Science measurement requirement	Instrument performance requirement
MR1. High spatial resolution measurement of the coronal magnetic field up to at least $3R_S$	**IR1.** Spatial resolution of a few arcsec; FOV from 1.15 to at least $3R_S$
MR2. High spatial resolution of electron density with FOV up to at least $3R_S$	**IR2.** Spatial resolution of a few arcsec; FOV from 1.15 to at least $3R_S$
MR3. Coronagraph data should have a temporal resolution of a few min to study dynamics	**IR3.** Up to 5 min resolution for CMEs in both phase 1 and 2, with proper trade-offs (pixels/compression)
MR4. Appropriate vantage point to measure all relevant physical quantities for Earth-directed CMEs	**IR4.** Part of science should be performed off Sun–Earth line, cf. mission requirements & profile
MR5. Coronagraph observations should provide measures at several temperatures	**IR5.** Measurements in both white light and UV (e.g., Lyman-α line) at least are needed
MR6. Wide-angle heliospheric imaging in white light for Sun-to-Earth tracking	**IR6.** FOV from close to the Sun and all the way to Earth at L5: from a few ° to ~70°
MR7. Sufficient spatial and temporal resolution for dynamics, a function of distance from Sun	**IR7.** FOV of at least 512 × 512 pixels. Cadence from 15 to 60 min depending on distance from Sun
MR8. Polarization measurements in wide-angle heliospheric imagery for accurate trajectory	**IR8.** Polarization shall be performed at least for three well-separated angles: e.g., −60°, 0°, +60°
MR9. Heliospheric polarization measurements only needed in outer FOV for tracking	**IR9.** Polarization measurement in heliospheric imagers only required beyond 20° from Sun
MR10. Need ion and magnetic field data at L1 for in-situ comparison	**IR10.** Magnetic field and plasma data are available from DSCOVR, ACE, Wind, etc.
MR11. Need ion and magnetic field data at INSTANT for in-situ comparison	**IR11.** Magnetic field and proton density, speed and temperature, with at least 1 min cadence
MR12. High-energy particles, in the keV to MeV range, with a sufficient time resolution to study SEPs from flares and CME-driven shocks	**IR12.** Electrons (20 keV–15 MeV), protons (20 keV–105 MeV), heavy ions (19–210 MeV/nuc), all with at least 1 min cadence

validated by coronagraphs located in the vicinity of the Earth, which best observe structures propagating at 60–90° off the Sun-spacecraft line. Coronal magnetic field measurements are thus required at significant distances off the Sun–Earth line, with the additional advantage to permit the reconstruction of the coronal properties facing the Earth.

2.1.2. *Measuring the coronal structure associated with CME initiation processes*

The Sun–Earth system gravitational L5 Lagrange point, as a stable vantage point, constitutes an optimum location from which to observe Earth-directed CMEs, in particular to determine the coronal magnetic field configuration associated with these eruptions (e.g., Cremades and Bothmer, 2004; Vourlidas et al., 2012).

In erupting structures and above active regions, emission in the Lyman-α line is much higher than the ambient coronal value, allowing for magnetic field measurements based on the Hanle effect with high spatial resolution (MR1). The twist signature of a flux rope within the CME may be detectable through the alignment of opposite polarities within the flux rope, i.e., the maps of the magnetic field direction would show alternating fields consistent with a flux rope structure (e.g., North–South or South–North polarities). An illustration of a possible magnetic topology during CME lift-off is given in Fig. 2b; discerning such a magnetic structure from actual observations would represent a significant advancement in the field. Confirmation of the CME flux rope existence further requires white-light measurements (for electron density estimates) in the same FOV, with similarly high spatial resolution. Such observations would constrain the overall morphology and possible presence of a compressed region or shock. This constitutes a second key measurement requirement (MR2; cf. summary in Tables 2 and 3). Both the magnetic field (Lyman-α) and density (white-light) estimates need to be obtained at a sufficient temporal resolution, typically at least 5 min (based on a fast CME passage in the field-of-view), to capture the underlying dynamics such as the evolution of the flux rope structure during the eruption (MR3). Combined with modeling and reconstruction techniques, such as what is being undertaken with CoMP currently (K. Dalmasse, private communication), such measurements will enable the prediction of the magnetic structure of the flux rope upon eruption, and thus its southward magnetic field component (B_z), the key parameter for generating geomagnetic storms. Making such estimates for Earth-directed CMEs requires that these coronagraph observations be made from a vantage point away from the Sun–Earth line (MR4). This constitutes a prime novelty of INSTANT.

The ability to distinguish between different CME initiation models would uniquely benefit from such combined Lyman-α and white-light observations (MR1, MR2, MR5) as they provide crucial information on a number of other CME model features: e.g., the presence of cavities, the extent of the compression region, and the location of current sheets and likely null points (e.g., reviews of CME properties by Chen (2011) and Webb and Howard (2012)). By providing coronal magnetic field and density measurements, the INSTANT concept provides a direct assessment of current CME initiation models. The cruise period towards L5, with higher telemetry, is well suited to accomplish this task, and the experience in calibration and data processing enables optimization studies for observations farther at L5. When at L5, INSTANT will provide the opportunity to compare Earth-bound CME initiation and magnetic structure observations with associated in-situ measurements near Earth and elsewhere in the heliosphere.

2.2. *What controls CME acceleration and subsequent propagation in the inner heliosphere?*

In the low β corona, the restructuring of the magnetic field dictates the dynamics of a CME by (1) setting the properties of the internal magnetic field of the CME, which generates the outward Lorentz force, and (2) altering the confining properties of the ambient coronal field through which the CME propagates. Studying CME kinematics in the low corona thus gives unique information on the net force acting on the CME during its formation and, therefore, the magnetic energy injected into the CME.

Tracking CMEs farther through the inner heliosphere is crucial for understanding CME interaction with the ambient solar wind, co-rotating interaction regions (CIRs) and even other CMEs. These interactions can change CME kinematics and trajectories, and alter their shape and overall orientation (e.g., Zuccarello et al., 2012; Lugaz et al., 2005; Ruffenach et al., 2012, 2015; Liu et al., 2014). A pivotal question in studying the Sun-to-Earth propagation of CMEs is how to disentangle CME kinematics from projection and

geometric effects. Accurate CME kinematics derivations need novel measurements, and the benchmarking of the inferred dynamics requires concurrent in-situ measurements in the inner heliosphere (e.g., Earth and L5).

2.2.1. Connecting coronal magnetic field restructuring with early CME dynamics

Current research typically acts on the assumption that CMEs originate from the destabilization of the coronal magnetic field that might have involved the formation of a flux rope, and that the subsequent acceleration is driven by strong magnetic forces and pressure gradients (e.g., Chen, 1989; Kliem and Török, 2006). However, the restructuring of the coronal magnetic fields that make up the CME and alter its surrounding environment is poorly understood. Measuring coronal magnetic fields in the vicinity of CME eruptions (with a temporal resolution of a few min) is key to providing groundbreaking results in this regard (MR3). A special focus on both magnetic and plasma pressure gradients in the corona, out to at least $3R_S$ (MR1), is vital owing to the presence of strong neighboring magnetic fields. High spatial resolution magnetic field measurements (to derive gradients) (MR1), together with similar white-light imaging capabilities (MR2) are needed to derive the underlying processes of the CME impulsive acceleration phase and to provide the crucial context information on how the ambient magnetic field configuration controls and reacts to this early-evolution phase.

INSTANT allows us to directly connect CME kinematics (white light) with observed coronal magnetic field configurations (Lyman-α). The cruise is best geared to fully constrain early CME dynamics, as well as to optimize measurements at L5. At L5, early CME dynamics is determined and combined with wide-angle imagery for the tracking of Earth-bound CMEs (next sections).

2.2.2. Disentangling CME Sun-to-Earth kinematics from projection and geometric effects

White-light data yield the total intensity of CME structures, i.e., their intensity integrated along the line of sight. To derive CME kinematics from wide-angle imagery, methods have been developed to convert the measured elongation angle (cf. STEREO Heliospheric Imagers in Fig. 3) to radial distance (e.g., Lugaz et al., 2009; Liu et al., 2010a, 2010b; Davies et al., 2012). These methods rely on ad-hoc assumptions of an ideal CME geometry. Wide-angle observations are needed to determine the propagation characteristics of CMEs from as close to the Sun as possible, all the way to the Earth (MR6) where their properties and impact effects can be studied using in-situ measurements (cf. Section 2.2.3). As shown by STEREO (e.g., Savani et al., 2009, 2010), such observations should have a sufficient spatial and temporal resolution for appropriate study of CME dynamics, with the highest resolutions close to the Sun (MR7).

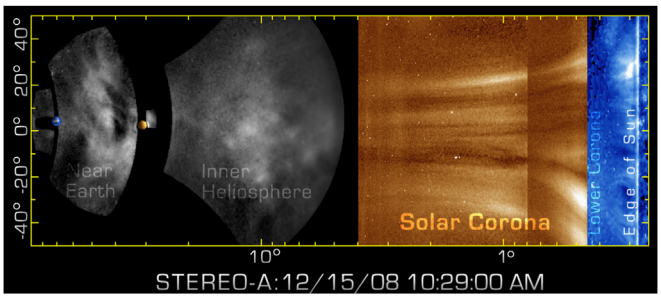

Fig. 3. Remote-sensing measurements in white light all the way from the corona (right-hand half of image) to the Earth (left blue body), as made by STEREO-A. Such wide-angle imaging has demonstrated the ability to track CMEs all the way to Earth and beyond (courtesy C. DeForest). (For interpretation of the references to color in this figure legend, the reader is referred to the web version of this article.)

Fully disentangling projection effects to study the 3D properties of CMEs from a single viewpoint requires measurements beyond total brightness, namely polarization information. This capability was demonstrated with SOHO/LASCO C2 and STEREO/COR2 polarization data covering distances up to $15R_S$ (Moran and Davila, 2004; de Koning and Pizzo, 2011). INSTANT will pursue this path to the next step by expanding the distances at which polarization measurements are made, up to $200R_S$ and beyond, thus being the first mission to make polarization measurements in wide-angle FOV heliospheric imaging (MR8). This approach has been investigated theoretically by Howard et al. (2013, and references therein).

While this polarization information may be of use for all elongation angles within the wide-angle FOV, the need for polarization measurements is most critical in the outer portion of the FOV where the viewing angle geometry varies the most (MR9). Indeed, the main reason for adding polarization to heliospheric imagers is that the use of pB/B (ratio of polarization brightness to total brightness) measurements permits locating features along the line of sight (Howard et al., 2013). Unlike the case of a coronagraph, if the feature can be tracked far enough, it is possible to resolve the front/behind ambiguity that otherwise exists owing to line-of-sight integration (MR7). Without relying on assumptions, such polarization information offers new clues to determine at what distance CME processes such as deflection occur and stop, how far from self-similar the CME expansion is, and how CMEs interact with solar wind structures and other CMEs. In addition, CME detection is easier with polarization brightness images as the behavior of the background (F-corona/Zodiacal light) is both predictable and sufficiently different from the features we want to measure (K-corona/solar wind) to warrant its easy subtraction (Calbert and Beard, 1972; Hayes et al., 2001).

2.2.3. Comparing CME remote-sensing characteristics with in-situ measurements

The previous science objectives were primarily arguing for innovative observations of the corona and heliosphere, in order to identify so far unknown properties of the corona, CMEs and their propagation in the inner heliosphere. However, a critical aspect remains the ability to compare the inferred CME magnetic and plasma structure (from MR 6–9) with actual in-situ measurements in the heliosphere thanks to the wide-angle heliospheric imaging. Doing so requires systematic in-situ measurements in the heliosphere at a location that is consistent with the direction of the CME leaving the Sun in the FOVs of a coronagraph and wide-angle imagers. For that purpose, only a location near L5 (MR4), with a side-on view of Earth-directed CMEs, makes it possible to systematically compare predicted CME properties with in-situ magnetic field and plasma observations at L1 (MR10) (e.g., Möstl et al., 2009; Liu et al., 2010b, 2011, 2013; Rouillard et al., 2011; Webb et al., 2012). The study of CMEs directed in between Earth and L5 would strongly benefit from in-situ ion and magnetic field data at the observing spacecraft (MR11).

INSTANT offers the possibility of confirming the presence of CME substructures (shock, sheath, flux rope) by connecting coronal and heliospheric imaging with in-situ observations at 1 AU. Comparison of CME properties with in-situ data at both L1 and INSTANT is possible at all times in the proposed scenario.

2.3. Where do CME-driven shocks form and how do their properties affect particle acceleration?

When CMEs expand rapidly in 3D, they can generate pressure waves that may steepen into shocks. Shock formation depends on the Alfvén speed and the CME bulk acceleration profiles; while the

Alfvén speed is believed to peak around 3 R_S (Gopalswamy et al., 2001), CME bulk acceleration typically occurs below $3R_S$ (Temmer et al., 2008; Bein et al., 2011). Previous studies have also shown that shocks can form low in the corona, down to $1.2R_S$ (Liu et al., 2009; Gopalswamy et al., 2013). However, no accurate observations of the shock-related magnetic field exist there. New ways for simultaneously determining the magnetic field and density in this region (and, hence, the Alfvén speed), as well as the CME acceleration profile, are needed to determine the shock formation height and properties. Depending on the acceleration profile of CMEs, shocks can also form at heights beyond $3R_S$ where the Alfvén speed starts declining. Our goal, however, is to focus on early shock formation since no observational methods are known to measure coronal magnetic fields above $3R_S$.

The properties and formation height of CME-driven shocks are critical to understanding solar energetic particle acceleration and their impact on the heliosphere (e.g., Reames, 2013). The current thinking is that one of the sources of high-energy particles is acceleration at these shock waves or in the highly compressed regions between the shock and the driver gas (the CME sheath). The particles are then subsequently channeled along the interplanetary magnetic field to 1 AU. Enhancing our understanding of the production of energetic particles during early CME-driven shock formation requires new capabilities: namely simultaneous measurements of the coronal magnetic field, coronal density distribution, early CME speed profile, as well as energetic particles in-situ at a location in the heliosphere that is magnetically connected to the particle source region.

2.3.1. *Determining shock formation and properties*

Although shocks have been inferred in the corona through type II radio bursts, there are currently only few direct observational means to study shocks in the low corona. We observe density jumps on the outer edges of expanding CMEs in extreme ultraviolet and white-light images (see Fig. 4a) and use indirect methods (tracking/modeling) to determine if a shock has occurred at the inferred location (e.g., Liu et al., 2009; Rouillard et al., 2012). A pressure wave steepens into a shock if its speed exceeds the characteristic speed of the medium where it propagates, here the Alfvén speed. Therefore, to ascertain whether a pressure wave is a shock or not, the background magnetic field (from Lyman-α) and density (white light) which control the characteristic speed of the ambient medium need to be measured (MR1, MR2). Owing to the dynamic nature of shocks, a temporal resolution of typically at least 5 min is required (MR3). The reconstruction of shock height (Fig. 4b) could then be compared with estimates based on routine radio type II burst measurements made from the ground (Sheeley et al., 2000; Liu et al., 2009).

The ambient magnetic field upstream of the shock is also important to understanding shock properties. Magnetic field reconstructions based on actual magnetic field measurements (MR1) would enable the determination of the geometry of the shock, as well as providing insights into the properties of both the upstream and downstream regions of the shock in the low corona. These properties determine in particular the obliqueness of the shock formed as a function of location; whether a shock is quasi-perpendicular or quasi-parallel is critical to particle acceleration, as discussed next in Section 2.3.2.

A more global understanding of shock formation and propagation requires tracking the shock structure as it evolves further out in the heliosphere. For that purpose, wide-angle imaging further away from the Sun (MR6) with sufficient spatial and temporal resolutions (MR7) is needed. Also, for proper tracking of the shock, polarization information in white light (MR8, MR9) brings the required enhanced accuracy for detailed reconstruction of their evolving properties.

With the MAGIC instrument (cf. Section 3), INSTANT provides the first combined measurements of coronal magnetic field, density and CME speed to determine CME-driven shock formation height and key properties (e.g., Alfvén Mach number, shock angles). Moreover, with polarized heliospheric imagery from PHELIX (cf. Section 3), INSTANT will better constrain the shock geometry and expansion throughout the inner heliosphere.

2.3.2. *Measuring energetic particle spectra in relation to shock height and properties*

The factors controlling the acceleration by shocks and subsequent transport of energetic particles are still a matter of active research. The maximum particle energy attainable during diffusive shock acceleration depends not only on the shock speed but also on the angle between the upstream magnetic field and the shock normal. Indeed, quasi-perpendicular shocks are thought to accelerate particles faster than quasi-parallel shocks and are strong candidates for the acceleration of the highest energy particles (e.g., Pesses et al., 1982; Reames, 1999; Lee et al., 2012).

For CMEs propagating towards the Earth, an observer at L5 is magnetically connected to the nose of the shock when the CME and shock are close to the Sun, owing to the Parker spiral

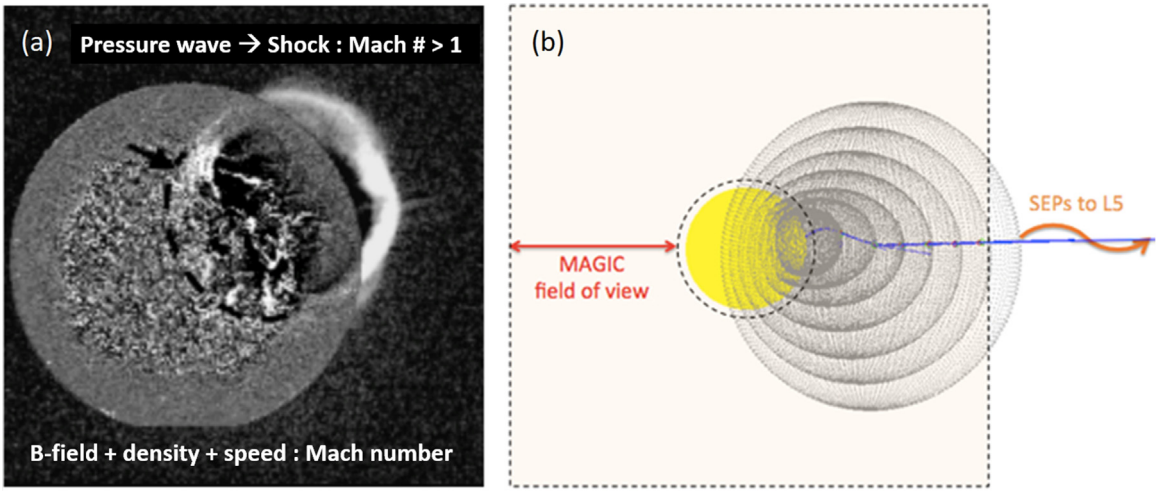

Fig. 4. (a) Composite image from STEREO during the launch of a CME. INSTANT will provide much richer white-light and Lyman-α images of the low corona where CME-driven shocks form, as well as coronal magnetic field measurements. (b) Illustration of the reconstruction of the shock structure which is made possible based on coronagraph observations up to $3R_S$ (the dashed box) on INSTANT (Figures courtesy of A. Rouillard).

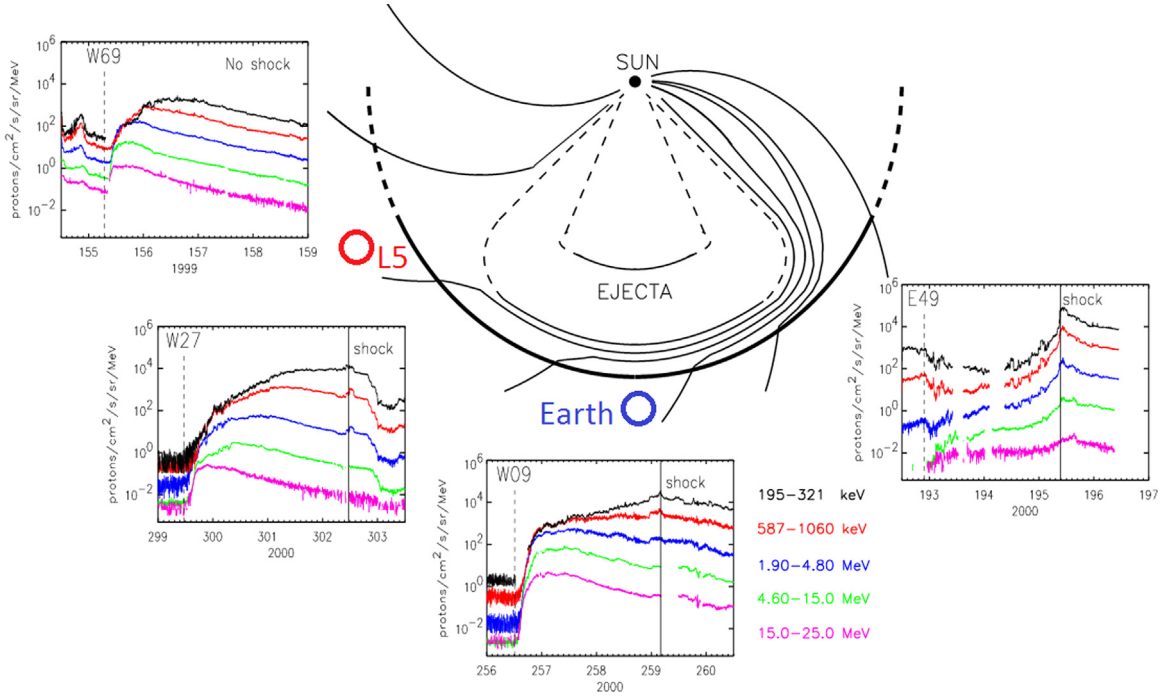

Fig. 5. Illustration of the longitudinal distribution of Solar Energetic Particles (SEPs), as a function of the connectivity to the CME-driven shock surface, for the case of an Earthbound CME. The four SEP charts correspond to the approximate position of the observer relative to the CME displayed. Note that the W/E letters in the flux panels correspond to the longitudes of the parent flares, not the position of the observer. This figure was adapted, in the context of the present mission concept, from a figure courtesy of D. Lario (Lario et al. (2004); cf. also Cane et al. (1988) and Reames (1999)).

geometry of the interplanetary magnetic field (MR4). Energetic particle measurements near L5 are thus crucial to provide the release times, fluxes and spectra of the earliest high-energy particles propagating along the magnetic field lines connected to the nose of the Earth-bound CME-driven shocks where they are produced (e.g., Reames, 1999). Measurements of electrons, protons, and heavier ions in the keV to MeV range with good time resolutions (of the order of a minute) are needed to study particles produced there (MR12). Comparing particle release times with the timing and height of shock formation from coronagraph and heliospheric imaging is crucial to constrain the coronal conditions that have produced the energetic particles measured in-situ (at L1, L5 and elsewhere; Fig. 5). This includes the determination of the regions of the greatest compressions close to the rapidly expanding CME, which have recently been suggested as major contributors to particle acceleration (e.g., Kozarev et al., 2013). At present this crucial information is available only through modeling of the coronal magnetic field (e.g., Kozarev et al., 2015). Comparisons of the time variation of particle fluxes and spectra with actual observations of the shock height and geometry (MR1, MR2, MR3) are needed to determine the importance of these parameters on high-energy particle production.

As a CME propagates, the geometry of the shock connected to the observer changes (e.g., Reames (1999); cf. Fig. 5). A combination of the novel remote-sensing and in-situ observations, enhanced by numerical modeling of particle transport, can provide new clues on how the energetic particle fluxes and spectra change for evolving shock geometry. To compare the global structure of the shock with its local structure in a systematic way, one needs to contrast the in-situ energetic particle measurements with accurate observations of the shock at larger heliocentric distances (wide-angle polarizing heliospheric imagers: MR6, MR7, MR8, MR9). Finally, synergy between particle measurements at L5 (MR11) and other locations (e.g., L1, MR10) leads to crucial information on the longitudinal variability of solar energetic particle events (Fig. 5).

2.4. How do observations at L5 increase our space weather prediction capabilities?

L5 is a gravitationally stable point in the Sun–Earth system and trails the Earth in its orbit by 60°. A vantage point from L5 enables the continuous monitoring of the Sun and the whole space along the Sun–Earth line, offering exceptional potential for both basic solar and heliospheric physics and space weather forecasting purposes. Below we identify critical space weather capabilities enabled by all the identified measurements requirements (MR1 to MR12), and making INSTANT an optimal sit-and-stare platform. The INSTANT concept thus can serve as a pathfinder for future space weather missions at L5.

2.4.1. Advance determination of geo-effective B_z component within CMEs

Although many processes are involved in the determination of CME geo-effectiveness (e.g., Lavraud and Rouillard, 2014; and references therein), the southward component of the interplanetary magnetic field (negative Bz) is key to the triggering of geomagnetic storms. The L5 location is ideal for early determination of the magnetic field structure of Earth-directed CMEs. With INSTANT, the radial and latitudinal profiles of the horizontal coronal magnetic fields can be estimated to reconstruct a plane-of-sky cross section of coronal magnetic field structures. Thus the orientation and helicity of a flux rope CME directed towards the Earth may be predicted. Further, methodologies will be developed to first predict the magnetic field arriving at the Earth through simple ballistic solutions. More advanced techniques that can integrate the PHELIX data to adjust the predictions according to evolutionary effects can be developed through the life cycle of the INSTANT mission. These techniques and forecasted data can be used to help develop an early warning of large geomagnetic storms. Even a very crude magnetic vector forecast at this stage is a very significant space weather forecasting improvement.

Table 4
Instrument measurement type, range, cadence, and associated requirements.

Instrument	Measurement	Range	Cadence	Requirements
MAGIC	Lyman-α and white-light coronagraph	1216 nm 5600 nm FOV: 1.15–3R_S	Phase 1: 5/30 min Phase 2: 5/30 min	**MR1, MR2, MR3 & MR5**
PHELIX	PHELIX-1 and PHELIX-2 white-light wide-angle imaging	PHELIX-1: 630–730 nm PHELIX-2: 400–1000 nm FOV: 3.75–70°	Phase 1: 15/20 min Phase 2: 30/60 min	**MR6, MR7, MR8 & MR9**
PAS	Ion distributions	50 eV–40 keV	1 min (up to 36 s)	**MR11**
MAG	Magnetic field	−128 to +128 nT	1 s (up to 20 Hz)	**MR11**
HEPS	Energetic particles:		1 min (up to 6 s)	**MR12**
	Electrons	20 keV–15 MeV		
	Protons	20 keV–105 MeV		
	Heavy ions	19–210 MeV/nuc		
IDPU	Data processing	N/A	N/A	**N/A**

2.4.2. Advance warning of the arrival of Earth-directed CMEs

The successful performance of the heliospheric imagers on STEREO demonstrated that a CME can be imaged in white light from the Sun all the way to the Earth and beyond (see Fig. 3). Using various techniques (e.g., Liu et al. 2010a, 2010b; Davies et al., 2012; Möstl et al., 2014) the arrival time and speed of Earth-directed CMEs can be predicted days before they reach the Earth. Additional polarization measurements first enabled by PHELIX permit a more accurate tracking of CMEs and their shocks, and thus will significantly improve predictions.

2.4.3. Advance in-situ measurements of CIRs before they pass the Earth

Corotating Interaction Regions (CIRs) are periodic spiral-like structures formed in the inner heliosphere as a result of interaction between fast and slow solar winds. CIRs are frequent drivers of shocks and recurrent geomagnetic storms. Because CIRs rotate in the direction of planetary motion, they sweep past L5 about 4.5 days before their arrival at Earth. CIRs are typically followed by high speed streams (HSS) intervals which drive prolonged geomagnetic activity and cause strong high-energy particle enhancements in the Earth's radiation belts (e.g. Reeves et al., 2003; Miyoshi et al., 2013; Kilpua et al., 2015). The efficiency of CIRs and HSS to accelerate radiation belt electrons depends for instance on the peak speed and density. Advance L5 measurements of CIR and HSS properties would be most critical for predicting radiation belt enhancements (Turner and Li, 2011). The in-situ measurements made by the MAG, PAS and HEPS instruments on INSTANT at L5 can be used to evaluate the magnetic field, plasma and energetic particle properties of these structures.

2.4.4. Advance warning of solar energetic particle events

Solar Energetic Particles (SEPs) can be produced by flares and/or CME-driven shocks and tend to propagate along magnetic field lines from their source regions. The Parker spiral magnetic field connects the L5 point to the central meridian from the Earth's view. From L5 one can measure the energetic particles from the nose of shocks driven by Earth-directed CMEs very close to the Sun, and thus in advance compared to observations made at Earth. Therefore, an L5 spacecraft provides advance warning of shock-related SEPs (electrons and ions), in addition to the driving CME properties obtained from the MAGIC and PHELIX imagers (Fig. 5).

2.5. Summary of scientific requirements

The science traceability matrix in Table 2 provides a mapping of the measurement requirements onto the science objectives and subtopics, as identified previously. Table 3 then summarizes how these measurement requirements (MR) translate into instrument performance requirements (IR). These IRs should be taken as suggestive performance requirements, given the MR. They are not further motivated here as they come from instrumental expertize within the INSTANT team.

3. Instant payload

3.1. Payload summary

The baseline INSTANT payload is listed in Table 4. The table includes basic measurement and telemetry needs for the instruments, and how these provide compliance with the science measurement requirements. To satisfy science measurement requirements MR1 & MR3, the INSTANT payload includes the MAGIC coronagraph, which for the first time provides measurements from space of the coronal magnetic field from 1.15R_S to 3R_S, using polarization measurements in the Lyman-α line (through the Hanle effect). In compliance with science requirements MR2, MR3 & MR5, MAGIC also measures in the white-light domain, with polarization capability, to obtain electron density and mass distribution in the corona. The Polarizing HELiospheric Imager eXplorer on board INSTANT addresses the science measurement requirements MR6 to MR9. It does so thanks to a wide-angle FOV (out to 70° elongation from Sun center in the ecliptic plane) imaging in the white-light domain with polarization capabilities for unprecedented accuracy in CME trajectory, speed and mass distribution determination. The INSTANT baseline payload also comprises a set of three in-situ instruments, with an associated IDPU for calculating ion moments, data formatting and communication with the spacecraft. HEPS measures the energy spectra of energetic electrons, protons and heavy ions in energy ranges that correspond to those of particles accelerated at CME-driven shocks and flares, complying with science requirements MR12. PAS measures the 3D distribution function of solar wind ions with the required resolution. MAG measures the in-situ magnetic field at a cadence of 1 Hz at minimum. In compliance with the science requirements MR11, PAS and MAG measure the in-situ properties of CMEs, CIRs and other solar wind features propagating over INSTANT.

3.2. Payload accommodation

Fig. 6 shows the possible accommodation of all the INSTANT instruments on a small platform, which results from a feasibility study undertaken with industrial partners (cf. Section 4).

As shown in Fig. 6, the MAGIC instrument is located inside the payload-dedicated mechanical structure on the side of the spacecraft opposite to the main spacecraft engine. The payload structure is positioned such that it reduces mechanical constraints during launch. The FOV of MAGIC faces the Sun without obstruction. The

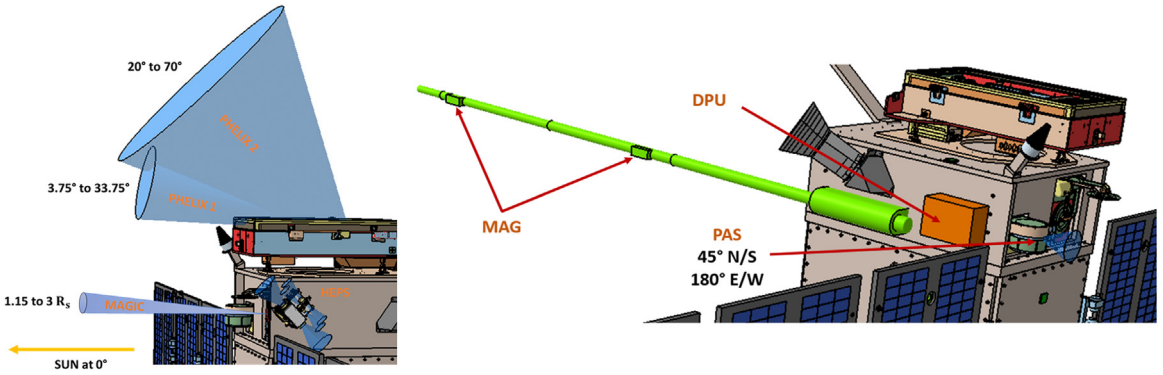

Fig. 6. Accommodation of the INSTANT payload, with FOVs marked with light blue cones for MAGIC, PHELIX, HEPS (left), and PAS (right). MAG is placed at two locations on the boom extending in the anti-Sunward direction from the spacecraft. (For interpretation of the references to color in this figure legend, the reader is referred to the web version of this article.)

PHELIX instrument is located on top of the structure containing MAGIC, and has the required FOV all the way from a few degrees to 70° without obstruction. The solar arrays extend in the north–south direction, relative to the ecliptic, so they don't interfere with the FOVs of PHELIX.

PAS protrudes through the top structure on the Sun-facing side to satisfy the need for its FOV to be sunward facing. HEPS is placed on the northward-facing side (relative to the ecliptic) of the top structure, close to the solar arrays. These arrays do not interfere with HEPS FOVs. The center of each of the FOVs of HEPS is directed 45° from the Sun in the ecliptic plane to align with the nominal Parker spiral orientation for a proper connectivity to the sources of energetic particles. MAG consists of two fluxgate units placed at two different locations along the boom which deploys on the shadow-side of the spacecraft. The two locations permit better calibration of spacecraft-induced magnetic fields. Finally, the IDPU is placed on a side of the top mechanical structure.

3.3. MAGIC: MAGnetic Imaging of the Corona

3.3.1. Instrument description

The proposed MAGIC (Fig. 7) coronagraph images the solar corona in Lyman-α (UV) and white-light (WL) bandwidths from 1.15 to 3R_S from Sun center with a resolution of 1.87 arcsec per pixel. MAGIC has a polarimetric capability in both channels to measure the magnetic field (UV) and isolate the Thomson-scattered corona (WL). The optical design is similar to that of LYOT (Vial et al., 2008), and of LASCO C1 on board SOHO, and a prototype already exists. The image of the Sun formed at the focal plane of the primary mirror runs through the annular secondary (M2) into a light trap (Fig. 7). The primary mirror mount includes three piezo-electric actuators allowing for the compensation of possible misalignments of the solar disk on the internal occulter. The image of the corona formed on the annulus is re-imaged by mirror M3 on the detectors via two folding flats (M4 & M5). The 8 cm aperture ensures short enough exposure times to correctly sample the dynamics of the corona.

In the UV channel, the polarization measurements are performed by combining a rotating 1216 nm 1/2 wave plate and a high reflectivity Brewster's angle linear polarizer. This latter uses an Al/MgF2 multilayer coating with 55% reflectivity and a polarizing power $>96\%$. It is mounted on a translation stage to switch to a non-polarizing second track to record total brightness. The back reflection from the front side of the wave plate is used to image the WL corona through a rotating dichroic linear polarizer. An orange filter located in front of the detector defines the WL passband. The two channels have the same 3072×3072 pixel, 10 μm pitch back-thinned Active Pixel Sensors (APS) passively cooled below -50 °C. The UV detector is coupled to a micro-channel plate (MCP) intensifier in order to maximize the SNR in Lyman-α.

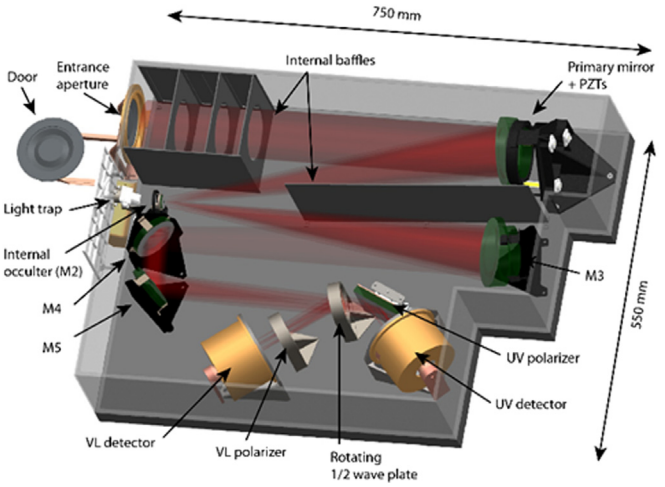

Fig. 7. Schematic of the MAGIC design with the various subsystems noted.

3.3.2. Performance and telemetry resources

The expected count rates and efficiencies of MAGIC were studied using measurements of components similar to those that will be used on MAGIC. The intensities were computed using a semi-empirical model of the corona. They are consistent with Lyman-α UVCS (UltraViolet Coronagraphic Spectrometer) observations on board SOHO. The range of exposure times corresponds to a signal-to-noise ratio SNR = 30 at 1.3R_S and SNR = 5 at 3R_S for a typical low coronal magnetic field strength; these are much improved for stronger fields in active regions and CMEs (Section 4.2). For magnetography, the SNR can be increased 4 times or more by binning the data (2×2, 3×3, etc.).

MAGIC is by far the most telemetry-demanding instrument of the INSTANT concept. Specific attention has thus been given to data products and ensuing telemetry requirements as a function of science phase. This is crucial given the constraints of the spacecraft system and orbit profile (cf. Section 4), which shows that 24 h ground contact with a deep space antenna provides a maximum of 120 kbps at L5 and an average ~450 kbps during phase 1 (cruise). Given the MAGIC performances, and the measurement and mission profile (Section 4), several MAGIC data products will be devised, such as for instance a high cadence product for times when CMEs are observed, and a lower cadence product for other times to study the static corona. Different binning and compressions can be

used to define these products during science phases 1 (cruise) and 2 (L5). Compatible with telemetry constraints, telemetry downlink rates of (phase 1) 95.4 kbps and (phase 2) 11.4 kbps can be achieved, satisfying the science objectives and requirements. These operations are performed in a separately mounted Data Processing Unit (DPU) connected to the spacecraft through SpaceWire interfaces.

Since the instrument works in the UV, it can be submitted to serious transmissivity degradation. Consequently, cleanliness measures (now well documented after more than 50 years of UV observations from space) must be taken at the different steps of project implementation. They may have some impact on overall budgets, but in compliance with instrument and spacecraft-level margins. Finally, as far as pointing requirements are concerned, the assumed small platform (PROBA-type) probably meets the stability and absolute accuracy requirements. If needed, a guiding telescope could be added or more simply the rejected image of the solar disk could be used for guiding.

3.4. PHELIX: Polarizing HELiospheric Imager eXplorer

3.4.1. Instrument description

The PHELIX instrument is based on the successful Heliospheric Imager (HI) instruments presently operating aboard the twin spacecraft of the NASA STEREO mission (Eyles et al., 2009). STEREO/HI on each spacecraft comprises two wide-angle white-light cameras mounted within a baffle system that provides sufficient rejection of solar stray-light background so that the propagation of CMEs through the heliosphere can be detected by means of Thomson scattering of photospheric light by free electrons in the K-corona. For the INSTANT mission concept, the original STEREO/HI capabilities would be enhanced by adding polarimetry and optimizing the FOV and cadence parameters.

The PHELIX design concept is displayed in Fig. 8. The PHELIX-1 and PHELIX-2 cameras have 30° and 50° circular FOVs, respectively, covering altogether a range of elongation angles (the angle away from Sun center) in the ecliptic plane from 3.75° to 70°, from as close to the solar limb as is feasible with the stray-light rejection used (given the overall constraints on size and mass of the instrument). The two cameras have an overlap region from 20° to 33.75°. The PHELIX-1 camera views over the top of the forward baffle assembly, which consists of a series of 5 linear "knife edge" baffles configured so that each baffle lies in the Fresnel diffraction rejection pattern of the preceding one. The PHELIX-2 camera lies within a set of deep conic-shaped baffles and has a polarizing filter mounted within a hollow-core stepper motor located just in front of its aperture (as done on previous coronagraphs such as on board SOHO). Well separated polarizer positions (e.g., here taken as −60°, 0° and +60°) relative to the ecliptic plane will be implemented. Image readout is by $2k \times 2k$ CCDs that are passively

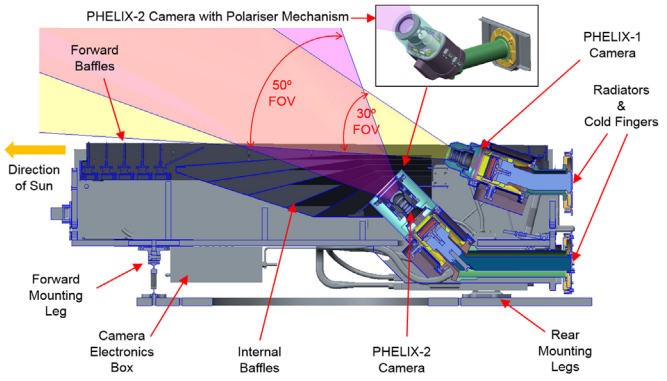

Fig. 8. Schematic view of the design of PHELIX with the various subsystems noted.

cooled to −60 °C or below by radiators facing deep space. A Camera Electronics Box (CEB) contains clocking and readout electronics for the CCDs and sends the images to a separately-mounted instrument Data Processing Unit (DPU) via SpaceWire interfaces.

3.4.2. Performance and telemetry resources

Performance parameters (resolution, cadence, TM) are less constrained than for MAGIC. In Phase 1, 15 and 20 min cadences are used for PHELIX-1 and PHELIX-2, respectively, with 1024×1024 images. Each PHELIX-2 exposure is actually a set of 3 exposures at the different polarizer positions. Allowing for 20 bits per pixel in the final summed exposure (to accommodate the large dynamic range of the cameras) together with a Rice compression factor of 2.2, we arrive at a telemetry downlink requirement of 26 kbps. At L5, in accordance with requirements, we implement 30 min and 1 h cadences for PHELIX-1 and PHELIX-2, respectively. Binning down to 512×512 image bins, i.e., sky bin sizes of 3.5 arcmin and 5.9 arcmin, gives 4 kbps. A burst mode product may be devised with 1024×1024 images, resulting in a 15.5 kbps telemetry requirement.

3.5. PAS: Proton and Alpha Sensor

The Proton and Alpha Sensor (PAS) on INSTANT measures the three-dimensional (3D) ion velocity distribution functions and its moments (velocity, density and temperature). PAS is composed of two main subsystems. One is the sensor head and the second is the electronics box. PAS has direct heritage from Chang'E-1/2 and other solar wind satellites worldwide.

The sensor head part consists of a deflection unit, a top-hat electrostatic analyzer, and micro-channel plates (MCPs) board with anodes. Arriving solar wind ions enter the instrument through an outer aperture grid. The deflector electrodes use a sweeping high voltage to steer ions from a desired arrival direction into the top-hat electrostatic analyzer (ESA). The top-hat electrostatic analyzer is made of two curved plates with a symmetric hemispheric shape. The inner hemisphere is polarized by a sweeping high voltage supply to select particles with specific energy through the analyzer. A chevron MCP stack is used for particle detection at the exit of the ESA.

The electronics unit consists of a preamplifiers unit, a high voltage unit, a housekeeping unit, an FPGA unit, a power supply unit and an interface unit. The latter is in charge of the communication between the instrument and the peripheral equipment, in particular with the In-situ Data Process Unit (IDPU) which performs moment calculations and data formatting and packaging.

3.6. MAG: MAGnetometer

MAG on INSTANT is a dual redundant digital fluxgate magnetometer consisting of two tri-axial fluxgate sensors connected by harness to a spacecraft-mounted electronics box. MAG has numerous heritage on past solar wind missions. To accurately measure the magnetic field, it is necessary to separate the ambient field from magnetic disturbances created by the spacecraft. To do this, the spacecraft needs to be as magnetically clean as possible and the sensors are mounted on spacecraft-provided rigid boom (nominally on the order of 3 m). Two sensors, mounted at different distances from the spacecraft on the boom, are combined to operate the sensors as a gradiometer and thus enable the background spacecraft magnetic field to be accurately subtracted from the measurements. The electronics unit consists of an FPGA with converter and dedicated front-end electronics for each of the two magnetometer sensors.

3.7. HEPS: High Energy Particle Sensors

The HEPS instrument combines two sensor heads and one electronics box in a resource-efficient package. Both sensors have two oppositely-pointing FOVs parallel/antiparallel to the nominal Parker spiral angle at 1 AU (45°). HEPS is essentially an adaptation of the EPT-HET sensor which has been developed and is currently being qualified for Solar Orbiter.

The Electron-Proton-Telescope (EPT) sensor head is based on the successful Solar Electron Proton Telescope (SEPT) on STEREO, but with improved electronics enabling a substantially lower energy threshold of 20 keV (instead of a de-facto ~80 keV; Müller-Mellin et al. (2008)). It combines the magnet-foil technique to separate electrons from protons. Each FOV consists of two apertures, leading to two pairs of closely-spaced solid-state detectors. Electrons up to 400 keV are deflected by a carefully balanced magnet system in one opening. In the other opening, protons below 400 keV are prevented from reaching the front detector by a thin deposition of parylene on the front of the detector.

The other HEPS sensor, the High-Energy Telescope (HET) is also an adaptation of Solar Orbiter's HET and is based on the Radiation Assessment Detector (RAD) of NASA's Mars Science Laboratory (MSL). It uses the multiple differential charge deposition versus total energy measurement technique to measure electrons, protons, and heavy ions over a large energy range (Hassler et al., 2012). Two solid-state detectors define the telescope FOV, which again points parallel/antiparallel to the nominal Parker spiral. Between these two pairs of detectors, a BGO (Bismuth Germanate) scintillator crystal serves as a calorimeter to measure the energy of the particles. The BGO crystal is read out by two photodiodes and stops protons up to 105 MeV and heavy ions up to ~210 MeV/nuc (species dependent). HEPS measures particles up to 210 MeV/nuc, and higher energies can be resolved up to a few hundred MeV/nuc. The entrance of both telescopes is covered by a light-tight aluminized kapton foil which reduces low-energy particles fluxes on the front detectors.

3.8. IDPU: In-situ Data Processing Unit

The IDPU serves as a central computer handling the commanding and telemetry for the three in-situ instruments: MAG, HEPS and PAS, implementing a single communication interface between the spacecraft and the three instruments. IDPU receives all relevant data products from HEPS, the raw counts from PAS and uncalibrated magnetic field vectors from MAG over digital links. It processes, reduces and compresses the data according to the instrument mode and transmits the final products to the spacecraft computer via a SpaceWire link. IDPU also manages the science modes of the instruments, including a burst mode when needed, and ensures synchronization and correct time-tagging of the data. IDPU also implements the on-board calculation of moments (density, velocity and temperature).

4. INSTANT mission profile

4.1. Launch and orbit strategy

In order to fulfill its science objectives (cf. Section 2), the INSTANT mission profile is designed to provide both (1) high-resolution, high-cadence measurements when relatively close to the Earth during cruise and (2) a full coverage of CMEs all the way from initiation to their impact on Earth, when the spacecraft reaches the L5 point which offers a stable viewing point off the Sun–Earth line. A small platform is injected into an escape orbit trailing the Earth and is then stabilized in an orbit around L5. The orbit design provides two distinct but complementary science phases. This strategy is based on the specific launcher and platform properties, as detailed next, which were investigated during a feasibility study with industrial partners.

4.1.1. Launch phase

Several launch vehicles have been envisaged for INSTANT. Most launch scenarios, e.g., Long March 2 C (with its third upper stage) or as a piggy-back passenger on either a Soyuz or Ariane 5, are achievable. A launch with a smaller Vega or LM-2D launcher appears less realistic owing to the need to escape Earth gravity.

4.1.2. Science phase #1 (1.5 years)

The launch vehicle will place the spacecraft on a heliocentric trajectory with the ellipticity allowing for a slow drift towards L5. Following a commissioning period, the first science phase of 1.5 years is conducted, benefiting from a high telemetry capability because of the relative proximity to Earth (see Fig. 11). In this phase the highest cadence and spatial resolution are achieved by the instruments, thereby permitting us to address several of the key science objectives before the telemetry drops significantly (cf. Section 4.3.3 and Fig. 11).

4.1.3. Thrusting phase and insertion at L5

The orbit optimization performed by industrial partners (Fig. 9) is based on a dual coast-arc/thrust strategy and provides a transfer to L5 on a time-scale of the order of 3 years with the use of a low thrust Electrical Propulsion (EP) system (as baselined for the platform in the present study). The ΔV of 0.808 km/s, necessary for stopping at L5, is then acquired after a ~1.3 year (467.63 days) thrusting period ending with a final insertion into a stabilized halo orbit around L5 with amplitude lower than 0.1 AU. Over this thrusting period, no science operations take place owing to a necessary rotation maneuver of the spacecraft (180°) for thruster alignment with the required delta-V vector.

4.1.4. Science phase #2 (1 year)

During this nominal 1-year phase, the payload instruments will operate continuously at their nominal level, benefiting from an accurate pointing capability (20 arcsec) provided by both the

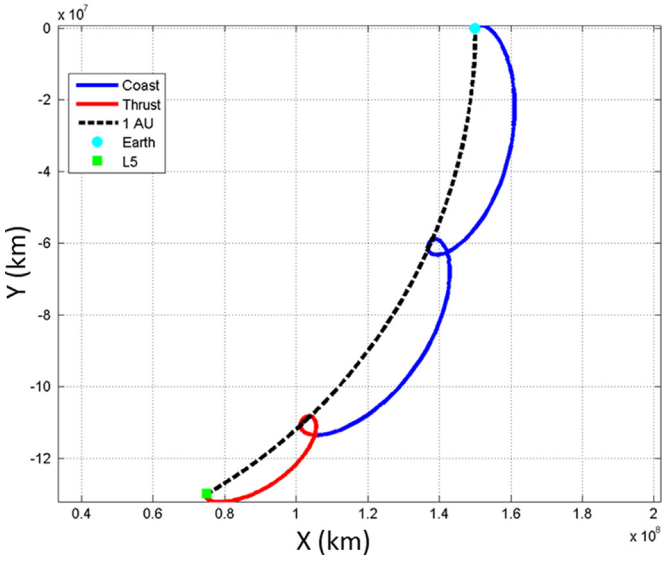

Fig. 9. INSTANT orbit strategy from Earth to L5 based on 3 years transfer depicted in a synodic frame. The blue coast arc is 628.12 days long. This multi-phase mission provides ample time for science operations prior to arrival at L5. The coordinates system is HEE (Heliocentric Earth Ecliptic), with axis values in km. The orbit is shown in the *X*–*Y* ecliptic plane. (For interpretation of the references to color in this figure legend, the reader is referred to the web version of this article.)

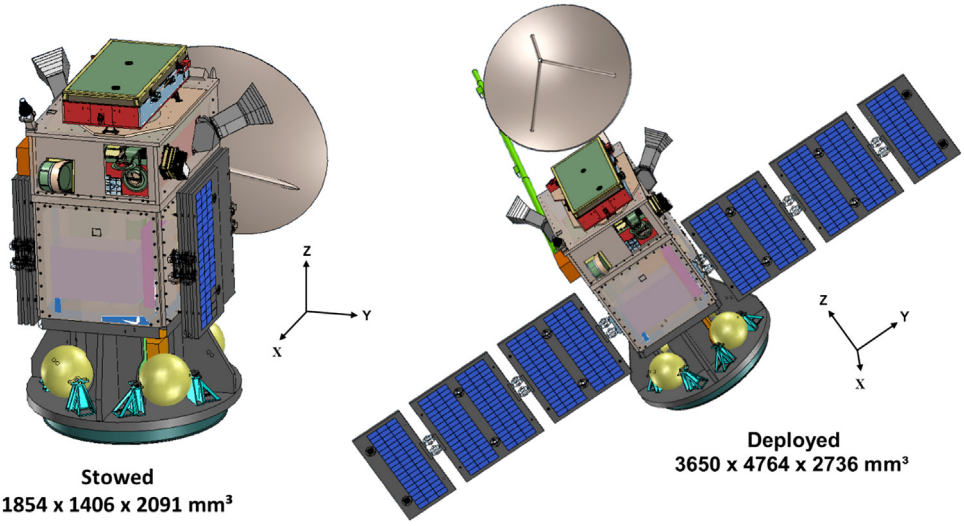

Fig. 10. Spacecraft in stowed and deployed configurations. Solar panels, HGA and boom are deployed during commissioning.

spacecraft and the orbit stability at L5. No Earth-shadowed (Earth-eclipsed) period will occur, permitting constant power supply from the Sun, so both science and telemetry operations can occur simultaneously at all times. Regarding the station keeping, a propellant allocation will be provided to manage the reaction wheels off-loading and station keeping. The L5 location permits unprecedented imaging and tracking of Earth-bound CMEs. Combined with in-situ measurements INSTANT will be able to accomplish a more complete understanding of how the magnetic structure and evolution of the corona influences Sun–Earth interactions. The stability of the L5 orbit combined with the propulsion margins on board the studied spacecraft and the constant power supplied by the Sun allow the possibility of continuing full science operations beyond the mission lifetime of 4 years (including 2.5 years of science operations) envisaged in the present scenario.

4.2. Micro-satellite platform study

4.2.1. Key drivers

The design studied with industry partners for the INSTANT concept is based on the re-use of the PROBA-NEXT (Project for On-Board Autonomy) platform, which has an extensive flight heritage of almost 20 years in orbit without failure on any of the launched satellites (PROBA-1, PROBA-2, PROBA-V).

The studied platform re-uses subsystems from existing small platforms, together with the maximum possible use of off-the-shelf equipment. Because PROBA is a microsatellite platform and, thus, has a limited volume, the propulsion subsystem needed for insertion at L5 must be sized accordingly. Based on the combined delta-V needs and limited volume available, an electric-based ion engine propulsion system was studied and designed based on previous flown systems (SMART-1).

The INSTANT spacecraft needs to cope with long distance (up to 1 AU) communication and operations. The telemetry, tracking and command (TT&C) subsystem must ensure a stable link, both during cruise and at L5, with the ground segment to support the instrument data downlink. To limit the burden on board the spacecraft (power and antenna diameter), the mission profile requires a ground station which hosts a large diameter antenna (of order 50 m) for downlink and uplink in X-band.

4.2.2. Spacecraft overview

Based on a PROBA platform, the proposed design provides a 3-axis stabilized spacecraft with highly accurate pointing capabilities. The additional EP system needed for the insertion at L5 constitutes a mass-saving design, providing more flexibility for attitude control of the platform during its cruise phase and for station keeping at L5.

The 6 payload elements (including IDPU) are accommodated within a dedicated structure, together with a 3 m foldable boom and a 1.1 m high gain antenna (HGA) both of which are deployed during commissioning. The spacecraft thermal control is mainly based on a passive strategy, using multi-layer insulation (MLI) coverage and radiative surfaces, but also active for the battery and propulsion subsystems.

Two solar arrays consisting of 3 deployable GaAs panels provide a maximum power supply of 588 W at 1 AU when facing perpendicular to the Sun, allowing for simultaneous science and telemetry operations. Finally, the dimensions of the stowed spacecraft (Fig. 10) can fit in most launcher fairings.

Although all spacecraft properties are not detailed here, the studied spacecraft dry mass is 277.1 kg, including a 20% margin at system level. All payload elements include a maturity margin ranging from 5% to 20% in line with their Technology Readiness Level TRL ≥ 6. The spacecraft wet mass accounts for a 19.1 kg of propellant mass required for L5 station keeping only. This results in a 296.2 kg spacecraft able to operate at L5 throughout the designed mission lifetime. The separate propulsion module required for transfer purposes has a dry mass of 121.9 kg (including a 20% system margin) and a wet mass of 166.8 kg, including the 44.9 kg of Xenon required to reach L5. The entire space segment weighs 563 kg. It includes the launch adapter (estimated at 100 kg) required to interface with the launch vehicle.

4.3. Ground segment operations

4.3.1. Overview of ground segment

As the telecommunication downlink operations at L5 are strongly constrained by significant attenuation in free space, the baseline downlink operations for INSTANT rely on the use of a large antenna ($\sim$50 m) together with a relevant spacecraft telecommunication subsystem designed to limit the burden on board the spacecraft. The studied scenario is fully realistic but further assessment may be performed to trade-off the transmitter power output with the HGA size and alternative ground station options.

The INSTANT spacecraft operates autonomously as soon as a target reference timeline is uplinked (using high-level commands), resulting in reduced operation costs for the ground segment

(including Mission Operation Center). The studied INSTANT mission profile thus benefits from the approved, low-cost approach used several times in the past PROBA missions. This also significantly reduces efforts for in-orbit commissioning and operations, resulting in a lower cost "phase E".

4.3.2. Spacecraft telecommunication subsystem

The telecommunication subsystem on board the spacecraft consists of a 1.1 m dish HGA working in X-band (supplied with 35 W) dedicated to the Telemetry operations (TM) throughout the nominal science operations. Two additional X-band LGAs provide a low telemetry communication mode (2 bps at 1 AU) which is sufficient for tracking and monitoring purposes during the thrusting phase, when only the ion thruster operates.

4.3.3. Science downlink operation scheme

Since the INSTANT spacecraft is designed to perform continuous measurements during all science phases, an evaluation of the maximum telemetry downlink capability (24/7 contact) along the entire orbit trajectory has been performed and is displayed in Fig. 11. The calculation in this figure is based on the Chinese deep space network (DSN) antenna (66 m) located in Jiamusi. Based on the characteristics of this antenna and of the spacecraft telecommunication subsystem, the calculated link budget provides 120 kbps downlink capability (for 24/7 contact with the ground antenna) with a comfortable link margin (>3 dB) under the worst case scenario at L5 (1 AU).

A 120 kbps downlink is not required for INSTANT at L5, given the fact that the MAGIC highest cadence data products (which are the most telemetry demanding) are only required during CME eruption within the MAGIC FOV. Only an average of one CME per day is expected (at most, for solar maximum) to occur in the MAGIC FOV. An upper limit for the required duration of the high cadence data product to be downlinked is obtained by simply assuming a slow CME, at average 400 km/s in the corona passing through the MAGIC FOV. With significant margins, this gives a conservative requirement of 3 h-duration high cadence data product per day. For the remaining 21 h of the day a lower cadence data product is downlinked. Given the telemetry needs for all instruments (not detailed here), in compliance with science measurements requirements, an average daily downlink of 18.9 kbps is needed when at L5.

The ground contact needed with the average link budget mentioned above is thus 4 hours per day for nominal science needs at L5. The same downlink strategy is planned for science phase 1, albeit with much lower constraints on the possibility to downlink higher cadence and higher spatial resolution data. Of course, there can be several CMEs during the same day in the MAGIC FOV, and no CMEs in the following day or several days. This is easily handled in the studied INSTANT design since all science data are recorded on the spacecraft-integrated mass memory, where up to 88 Gbits are available, corresponding to >10 days of nominal science operations at L5 at the rate of $\sim$60 kbps. Selection of the high-resolution data to be downlink, i.e., during CME eruptions, can be planned from ground using beacon data, and knowledge from other spacecraft and ground measurements. Onboard triggers may also be implemented. Finally, smaller antennas may be used for downlinking beacon data products in real time if space weather operational activities are planned.

5. Conclusions

We presented a small mission concept to the Sun–Earth Lagrangian L5 point. The proposed INSTANT mission concept is designed to address innovative solar, heliospheric and space weather science questions. The INSTANT concept would be the first to (1) obtain measurements of coronal magnetic fields from space, and (2) determine CME kinematics with unparalleled accuracy. Observations from the L5 location with the proposed innovative instrumentation would permit to uniquely track the whole chain of processes in Sun–Earth interaction. The INSTANT mission design can be considered as a pathfinder for more comprehensive or operational space weather missions at L5 (cf. Schrijver et al., 2015). The present study demonstrates that a mission addressing compelling science questions from L5 can be performed with a high TRL platform and payload within small mission programmatic constraints.

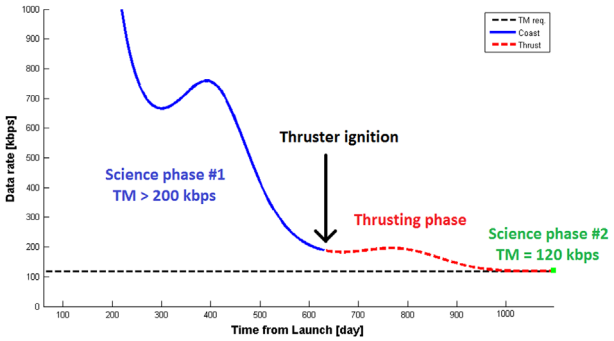

Fig. 11. Maximum telemetry budget, for 24 h/day downlink, along the cruise phase from Earth to L5, calculated based on the baseline spacecraft telecommunication subsystem and a large DSN antenna ($\sim$50 m).

Acknowledgments

The authors acknowledge the inputs and support from more than 180 collaborators to the INSTANT mission proposal submitted to the ESA and CAS call for small missions in 2015. Although INSTANT was not selected in that call, the concept will be proposed in future opportunities at ESA or other agencies. Work at IRAP was supported by CNES and CNRS. BL wishes to thank D. Lario for providing the figure from which Fig. 5 is adapted.

References

Akioka, M., Nagatsuma, T., Miyake, W., Ohtaka, K., Marubashi, K., 2005. The L5 mission for space weather forecasting. Adv. Space Res. 35, 65–69.
Amari, T., Aly, J.-J., Chopin, P., Canou, A., Mikic, Z., 2014. Large scale reconstruction of the solar coronal magnetic field. J. Phys. Conf. Ser. 544, 012012.
Arnaud, J., Roudier, T., Malherbe, J.-M., Moity, J., 2006. Solar spectro-polarimetry at Pic-du-Midi/LJR. In: Casini, R., Lites, B.W. (Eds.), Proceedings of the Solar Polarization 4, ASP Conference Series. p. 358.
Aschwanden, M.J., 2004. Physics of the Solar Corona: An Introduction, Published by Praxis Publishing Ltd., Chichester, UK, and Springer-Verlag Berlin, ISBN.3-540-22321-5.
Bein, B.M., et al., 2011. Impulsive acceleration of coronal mass ejections. I. Statistics and coronal mass ejection source region characteristics. Astrophys. J. 738, 191.
Bommier, V., Sahal-Bréchot, S., 1982. The Hanle effect of the coronal Lα line of hydrogen: theoretical investigation. Sol. Phys. 78, 157.
Calbert, R., Beard, D.B., 1972. The F and K components of the solar corona. Astrophys. J. 176, 497.
Cane, H.V., Reames, D.V., von Rosenvinge, T.T., 1988. The role of interplanetary shocks in the longitude distribution of solar energetic particles. J. Geophys. Res. 93, 9555.
Chen, J., 1989. Effects of toroidal forces in current loops embedded in a background plasma. Astrophys. J. 338, 453.
Chen, P.F., 2011. Coronal mass ejections: models and their observational basis. Living Rev. Sol. Phys. 8, 1.
Cremades, H., Bothmer, V., 2004. On the three-dimensional configuration of coronal mass ejections. Astron. Astrophys. 422, 307–322.
Davies, J.A., et al., 2012. A self-similar expansion model for use in solar wind transient propagation studies. Astrophys. J. 750, 23.
de Koning, C.A., Pizzo, V.I., 2011. Polarimetric localization: a new tool for calculating the CME speed and direction of propagation in near-real time. Space Weather 9, 03001.
Dere, K.P., 1996. The rate of magnetic reconnection observed in the solar atmosphere. Astrophys. J. 472, 864.

Derouich, M., Auchere, F., Vial, J.C., Zhang, M., 2010. Hanle signatures of the coronal magnetic field in the linear polarization of the hydrogen Lα line. Astron. Astrophys. 511, A7.
Eyles, C.J., et al., 2009. The heliospheric imagers onboard the STEREO Mission. Sol. Phys. 254, 387.
Fan, Y.H., 2015. MHD equilibria and triggers for prominence eruption. In: Vial, J.-C., Engvold, O. (Eds.), Solar Prominences 415; 2015, p. 297.
Forbes, T.G., et al., 2006. CME theory and models. Space Sci. Rev. 123 (1–3), 251–302.
Gary, G.A., 2001. Plasma Beta above a solar active region: rethinking the paradigm. Sol. Phys. 203 (1), 71–86.
Gibson, S., 2015. Coronal cavities: observations and implications for the magnetic environment of prominences. In: Vial, J.-C., Engvold, O. (Eds.), Solar Prominences 415; 2015, p. 323.
Gopalswamy, N., Lara, A., Kaiser, M.L., Bougeret, J.L., 2001. Near-Sun and near-Earth manifestations of solar eruptions. J. Geophys. Res. 106, 25261.
Gopalswamy, N., et al., 2011a. Earth-Affecting Solar Causes Observatory (EASCO): A mission at the Sun–Earth L5. In: Fineschi, S., Fennelly, J. (Eds.), Proceedings of Solar Physics and Space Weather Instrumentation IV, SPIE, 8148, p. 81480Z.
Gopalswamy, N., et al., 2011b. Earth-Affecting Solar Causes Observatory (EASCO): A potential international living with a star mission from Sun–Earth L5. J. Atmos. Sol.-Terr. Phys. 73, 658–663.
Gopalswamy, N., Yashiro, S., 2011. The strength and radial profile of the coronal magnetic field from the standoff distance of a coronal mass ejection-driven shock. Astrophys. J. Lett. 736, L17.
Gopalswamy, N., et al., 2013. The first ground level enhancement event of solar cycle 24: direct observation of shock formation and particle release heights. Astrophys. J. Lett. 765, L30.
Hassler, D.M., et al., 2012. The radiation assessment detector (RAD) investigation. Space Sci. Rev. 170, 503–558.
Hayes, A.P., Vourlidas, A., Howard, R.A., 2001. Deriving the electron density of the solar corona from the inversion of total brightness measurements. Astrophys. J. 548 (2), 1081–1086.
Howard, T.A., Tappin, S.J., Odstrcil, D., DeForest, C.E., 2013. The Thomson surface. III. Tracking features in 3D. Astrophys. J. 765, 45.
Kaiser, M.L., et al., 2008. The STEREO mission: an introduction. Space Sci. Rev. 136 (1–4), 5–16.
Kilpua, E.K.J., et al., 2015. Unraveling the drivers of the storm time radiation belt response. Geophys. Res. Lett. 42 (9), 3076.
Kliem, B., Török, T., 2006. Torus instability. Phys. Rev. Lett. 96, 255002.
Kozarev, K.A., et al., 2013. Global numerical modeling of energetic proton acceleration in a coronal mass ejection traveling through the solar corona. Astrophys. J. 778, 43.
Kozarev, K.A., Raymond, J.C., Lobzin, V.V., Hammer, M., 2015. Properties of a coronal shock waves as a driver of early SEP acceleration. Astrophys. J. 799, 167.
Lario, D., et al., 2004. Solar energetic particle variations. In: Pap, J.M., Fox, P. (Eds.), Solar Variability and its Effects on Climate, AGU Geophysical Monograph, 141, pp. 195–216.
Lavraud, B., Rouillard, A.P., 2014. Properties and processes that influence CME geo-effectiveness, Nature of Prominences and their role in Space Weather. In: Schmieder, B., Malherbe, J.-M., Wu, S.T. (Eds.), Proceedings of the IAU Symposium, 8, S300, pp. S273–S284.
Lee, M.A., Mewaldt, R.A., Giacalone, J., 2012. Shock acceleration of ions in the heliosphere. Space Sci. Rev. 173 (1–4), 247–281.
Lin, H., Kuhn, J.R., Coulter, R., 2004. Coronal magnetic field measurements. Astrophys. J. 613, L177.
Liu, Y., Luhmann, J.G., Bale, S.D., Lin, R.P., 2009. Relationship between a coronal mass ejection-driven shock and a coronal metric type II burst. Astrophys. J. Lett. 691, L151.
Liu, Y., Davies, J.A., Luhmann, J.G., Vourlidas, A., Bale, S.D., Lin, R.P., 2010a. Geometric triangulation of imaging observations to track coronal mass ejections continuously out to 1 AU. Astrophys. J. Lett. 710, L82.
Liu, Y., et al., 2010b. Reconstructing coronal mass ejections with coordinated imaging and in situ observations: global structure, kinematics, and implications for space weather forecasting. Astrophys. J. 722, 1762.
Liu, Y., Luhmann, J.G., Bale, S.D., Lin, R.P., 2011. Solar source and heliospheric consequences of the 2010 April 3 coronal mass ejection: a comprehensive view. Astrophys. J. 734, 84.
Liu, Y.D., et al., 2013. On Sun-to-Earth propagation of coronal mass ejections. Astrophys. J. 769, 45.
Liu, Y., et al., 2014. Observations of an extreme storm in interplanetary space caused by successive coronal mass ejections. Nat. Commun. 5, 3481.
Lopez-Ariste, A., 2015. Magnetometry of prominences. In: Vial, J.-C., Engvold, O. (Eds.), Solar Prominences 415; 2015, p. 179.
Lugaz, N., Vourlidas, A., Roussev, I.I., 2009. Deriving the radial distances of wide coronal mass ejections from elongation measurements in the heliosphere – application to CME-CME interaction. Ann. Geophys. 27, 3479.
Lugaz, N., Manchester IV, W.B., Gombosi, T.I., 2005. Numerical simulation of the interaction of two coronal mass ejections from Sun to Earth. Astrophys. J. 634 (1), 651–662.
Mackay, D., Yeates, A., 2012. The Sun's global photospheric and coronal magnetic fields: observations and models. Living Rev. Sol. Phys. 9, 6.
Mandrini, C.H., Demoulin, P., Klimchuk, J.A., 2000. Magnetic field and plasma scaling laws: their implications for coronal heating models. Astrophys. J. 530, 999.
Miyoshi, Y., et al., 2013. High-speed solar wind with southward interplanetary magnetic field causes relativistic electron flux enhancement of the outer radiation belt via enhanced condition of whistler waves. Geophys. Res. Lett. 40, 4520–4525.
Moran, T., Davila, T., 2004. Polarimetric three-dimensional imaging of coronal mass ejections. Bull. Am. Astron. Soc. 36, 683.
Möstl, C., et al., 2009. Linking remote imagery of a coronal mass ejection to its in situ signatures at 1 AU. Astrophys. J. 705, L180.
Möstl, C., et al., 2014. Connecting speeds, directions and arrival times of 22 coronal mass ejections from the Sun to 1 AU. Astrophys. J. 787, 119.
Müller-Mellin, R., et al., 2008. The solar electron and proton telescope for the STEREO mission. Space Sci. Rev. 136, 363–389.
Pesses, M.E., Decker, R.B., Armstrong, T.P., 1982. The acceleration of charge particles in interplanetary shock waves. Space Sci. Rev. 32 (1–2), 185–204.
Reames, D.V., 1999. Particle acceleration at the sun and in the heliosphere. Space Sci. Rev. 90, 413.
Reames, D.V., 2013. The two sources of solar energetic particles. Space Sci. Rev. 175, 53.
Reeves, G.D., McAdams, K.L., Friedel, R.H.W., O'Brien, T.P., 2003. Acceleration and loss of relativistic electrons during geomagnetic storms. Geophys. Res. Lett. 30, 1529.
Reid, G.C., 1986. Solar energetic particles and their effects on the terrestrial environment. Geophys. Astrophys. Monogr. 26, 251–278.
Rouillard, A.P., et al., 2011. Interpreting the properties of solar energetic particle events by using combined imaging and modeling of interplanetary shocks. Astrophys. J. 735, 7.
Rouillard, A.P., et al., 2012. The longitudinal properties of a solar energetic particle event investigated using modern solar imaging. Astrophys. J. 752, 44.
Ruffenach, A., et al., 2012. Multi-spacecraft observation of magnetic cloud erosion by magnetic reconnection during propagation. J. Geophys. Res. 117, A09101.
Ruffenach, A., et al., 2015. Statistical study of magnetic cloud erosion by magnetic reconnection. J. Geophys. Res. 120, 43–60.
Savani, N.P., et al., 2009. The radial width of a coronal mass ejection between 0.1 and 0.4 AU estimated from the heliospheric imager on STEREO. Ann. Geophys. 27, 4349–4358.
Savani, N.P., Owens, M.J., Rouillard, A.P., Forsyth, R.J., Davies, J.A., 2010. Observational evidence of a coronal mass ejection distortion directly attributable to a structured solar wind. Astrophys. J. Lett. 714, L128.
Schmidt, W.K.H., Bothmer, V., 1996. Stereoscopic viewing of solar coronal and interplanetary activity. Adv. Space Res. 17 (4/5), 369–376.
Schrijver, C., et al., 2015. Understanding space weather to shield society: a global road map for 2015–2025 commissioned by COSPAR and ILWS. Adv. Space Res. 55 (12), 2745–2807.
Sheeley, N.R., Hakala, W.N., Wang, Y.M., 2000. Detection of coronal mass ejection associated shock waves in the outer corona. J. Geophys. Res. 105, 5081.
Simunac, K.D.C., Kistler, L.M., Galvin, A.B., Popecki, M.A., Farrugia, C.J., 2009. In situ observations from STEREO/PLASTIC: a test for L5 space weather monitors. Ann. Geophys. 27, 3805–3809.
Strugarek, A., et al., 2015. A space weather mission concept: observatories of the solar corona and active regions (OSCAR). J. Space Weather Space Clim. 5, A4.
Temmer, M., et al., 2008. Acceleration in fast halo CMEs and synchronized flare HXR bursts. Astrophys. J. 673 (1), L95–L98.
Tomczyk, S., et al., 2008. An instrument to measure coronal emission line polarization. Sol. Phys. 247, 411.
Trujillo Bueno, J., Merenda, L., Centeno, R., Collados, M., Landi Degl'Innocenti, E., 2005. The Hanle and Zeeman effects in solar spicules: a novel diagnostic window on chromospheric magnetism. Astrophys. J. Lett. 619, L191.
Turner, D.L., Li, X., 2011. Using spacecraft measurements ahead of Earth in the Parker spiral to improve terrestrial space weather forecasts. Space Weather 9, S01002.
Vial, J.C., et al., 2008. SMESE (SMall Explorer for Solar Eruptions): a microsatellite mission with combined solar payload. Adv. Space Res. 41, 183.
Vourlidas, A., Lynch, B.J., Howard, R.A., Li, Y., 2012. How many CMEs have flux ropes? Deciphering the signatures of shocks, flux ropes, and prominences in coronagraph observations of CMEs. Sol. Phys. 284, 179.
Vourlidas, A., 2015. Mission to the Sun–Earth L5 Lagrangian point: an optimal platform for space weather research. Space Weather 13, 197–201.
Webb, D.F., et al., 2010. Using STEREO-B as an L5 space weather pathfinder mission. Space Res. Today 178, 10–16.
Webb, D.F., Howard, T.A., 2012. Coronal mass ejections: observations. Living Rev. Sol. Phys. 9, 3.
Webb, D.F., et al., 2012. Heliospheric imaging of 3-D density structures during the multiple coronal mass ejections of late July to early August 2010. Sol. Phys. 285, 317–348.
Zuccarello, F.P., Bemporad, A., Jacobs, C., Mierla, M., Poedts, S., Zuccarello, F., 2012. The role of streamers in the deflection of coronal mass ejections: comparison between STEREO three-dimensional reconstructions and numerical simulations. Astrophys. J. 744, 66.